Journal of Materials Chemistry A

ROYAL SOCIETY OF CHEMISTRY

COMMUNICATION

View Article Online
View Journal | View Issue

Cite this: J. Mater. Chem. A, 2026, 14, 385

Received 10th September 2025
Accepted 1st December 2025

DOI: 10.1039/d5ta07405c

rsc.li/materials-a

Efficient synthesis strategy of near-zero volume change materials for all-solid-state batteries operable under minimal stack pressure

Teppei Ohno,[a] Yosuke Ugata [ab] and Naoaki Yabuuchi [*ab]

All-solid-state batteries are promising for energy storage applications because of the high ionic conductivity of solid electrolytes. Nevertheless, high stack pressure is required during operation to accommodate electrode volume changes and to maintain interfacial contact. $Li_{8/7}Ti_{2/7}V_{4/7}O_2$ (LTVO) has been reported as a dimensionally invariable high-capacity positive electrode material. While the synthesis of LTVO typically necessitates high-energy ball milling to produce nanosized particles with large surface areas, thereby mitigating the sluggish electrode kinetics inherent to disordered structures, this process is unsuitable for mass production. In this study, LTVO samples with different surface areas are synthesized by tuning synthesis temperatures and post-milling treatment conditions and employing solution-based synthesis methods. The optimized sample (~20 m^2 g^{-1}) exhibits a large reversible capacity of ~250 mA h g^{-1}, and can be synthesized using a scalable approach. Furthermore, the optimized LTVO enables stable operation of all-solid-state batteries under minimal stack pressure (<0.5 MPa).

Introduction

Toward building a sustainable society through the maximum use of electric vehicles and renewable energy, the development of high-energy and safe lithium-ion batteries (LIBs) is urgently required.[1,2] Commercial LIBs employing flammable and volatile organic liquid electrolytes suffer from safety issues such as ignition and electrolyte leakage.[3] To overcome this issue, all-solid-state batteries (ASSBs) are considered as promising technology for energy storage applications. Solid electrolytes (SEs) such as Li^+ ion conducting sulfides and oxides are intrinsically non-flammable, thermally stable, and mechanically robust.[4] Moreover, various types of sulfide-based SEs with comparable ionic conductivity to liquid electrolytes have been reported, including $Li_{10}GeP_2S_{12}$ (12 mS cm^{-1} at 25 °C)[5] and $Li_{5.3}PS_{4.3}Cl_{0.7}Br_{1.0}$ (26 mS cm^{-1} at 25 °C).[6] Despite these advantages, ASSBs still face several challenges in practical applications. One of the most critical issues is the interface construction between electrode materials and SEs. In general, volume changes in electrode materials during lithium extraction and insertion lead to the formation of voids and cracks within the electrode–SE composites, resulting in the loss of interfacial contact, which significantly increases interfacial resistance and cell polarization.[7,8] To preserve intimate contact at the electrode–electrolyte interfaces, high stack pressures (>10 MPa) are typically applied during cell operation.[9] However, low stack pressures below 1 MPa are desirable for increasing pack-level energy density and facilitating mass production without the need for bulky pressure jigs.[10,11] Thus, developing effective strategies to ensure stable interfacial contact and reliable cycling performance under reduced pressure conditions is crucial for the widespread adoption of ASSBs.

Recently, electrode materials with small volume change have attracted significant attention as a key strategy for achieving long-lived ASSBs.[12–14] Among them, Li-rich metal oxides with cation-disordered rocksalt structures have emerged as promising candidates.[15–17] The disordered cation arrangement provides a rigid three-dimensional framework, enabling minimal volume change during the reversible extraction/insertion of a large amount of Li ions. For instance, $Li_{9/7}Nb_{2/7}Mo_{3/7}O_2$ and $Li_{5/4}Nb_{1/4}V_{1/2}O_2$ exhibit small volume changes of less than 2% during cycling, while delivering high reversible capacities of ~300 mA h g^{-1}.[18,19] These volume changes are significantly smaller than those observed in typical layered materials such as $LiCoO_2$ and $LiNiO_2$, which exhibit volume changes ~10% upon full delithiation.[20] Furthermore, the binary system of $xLi_2TiO_3 - (1-x)LiVO_2$, specifically for the sample of $x = 0.33$ ($Li_{8/7}Ti_{2/7}V_{4/7}O_2$), has been reported to show a near dimensionally invariable character during charge and discharge.[21] Notably, nanosized $Li_{8/7}Ti_{2/7}V_{4/7}O_2$ (LTVO) delivers

[a]Department of Chemistry and Life Science, Yokohama National University, 79-5 Tokiwadai, Hodogaya-ku, Yokohama 240-8501, Japan. E-mail: yabuuchi-naoaki-pw@ynu.ac.jp

[b]Advanced Chemical Energy Research Center (ACERC), Institute of Advanced Sciences, Yokohama National University, 79-5 Tokiwadai, Hodogaya-ku, Yokohama 240-8501, Japan

a high reversible capacity exceeding 300 mA h g^{-1} and demonstrates excellent cyclability without capacity fading over 400 cycles in all-solid-state cells with an argyrodite-type sulfide-based solid electrolyte, Li_6PS_5Cl. However, these cells were operated under a high stack pressure of 200 MPa, which is much higher than the ideal practical stack pressure. Moreover, nanosized LTVO was prepared by high-energy ball milling, which is unsuitable for large-scale production.

In this study, an optimized synthesis process for LTVO is explored to improve material production efficiency, and its applicability to ASSBs is examined under reduced stack pressure. A systematic study reveals that the particle size and surface area of LTVO are primary factors governing its reversible capacity as electrode materials. LTVO with the optimum particle size and surface area is successfully synthesized through a combination of lower synthesis temperature and efficient post-milling treatment. Additionally, solution-based synthesis, known for producing fine particles with high specific surface areas,[22] is also examined as an alternative approach. The electrode reversibility of the optimized LTVO sample with liquid and solid electrolytes is also compared. Due to suppressed dissolution of V ions, superior reversibility with the solid electrolyte is achieved even under minimal stack pressure. Based on these findings, design strategies for V-based Li-rich electrode materials with a disordered structure are discussed in detail for practical ASSB applications with reduced stack pressures.

Results and discussion

Solid-state synthesis of $Li_{8/7}Ti_{2/7}V_{4/7}O_2$ with the post-milling process

Fig. 1a shows XRD patterns of samples synthesized at different calcination temperatures from 600 to 900 °C. The samples calcined in the range of 700 to 900 °C exhibit well-defined diffraction lines, all of which can be attributed to the α-$NaFeO_2$-type layered rocksalt structure.[23] In contrast, splitting for the 003 diffraction line is observed for the samples calcined below 700 °C, suggesting the presence of $LiVO_2$ and Li_2TiO_3 as segregated phases. In addition, some of the additional peaks, which cannot be assigned to the layered rocksalt phase, are noted in the range of 20 to 30 degrees, and these peaks can be attributed to Li_2TiO_3 with in-plane cation ordering of Li and Ti ions.[24] These observations indicate that phase segregation cannot be suppressed in samples calcined below 700 °C. Single-phase LTVO samples can be synthesized above 700 °C from the precursor used in this study. Fig. S1 and S2 present SEM images of the samples synthesized at various calcination temperatures. The sample calcined at 900 °C contains relatively large particles of >5 μm whereas the sample at 700 °C consists of powders with smaller and uniform particle sizes of approximately 2 μm. The reduction in particle size is attributed to the suppression of particle growth during calcination at lower temperatures. Fig. 1b and S3 compare energy dispersive X-ray spectroscopy (EDX) mappings of Ti and V ions for the samples calcined at 650 and 700 °C. The distribution of Ti and V ions is uniform for the sample calcined at 700 °C, but partial segregation, as expected from the XRD data, is observed for the sample calcined at 650 °C. Therefore, the lower limit of the calcination temperature for LTVO is concluded to be 700 °C. To further optimize the calcination conditions, samples were synthesized at a fixed calcination temperature of 700 °C with shortened calcination times. The XRD patterns, SEM images, and EDX mappings of these samples are summarized in Fig. S4. A single-phase LTVO sample is successfully synthesized even when the calcination time is decreased to 3 h. However, further shortening the calcination holding time to 0 h at 700 °C is not successful to obtain a phase-pure sample. These results demonstrate that LTVO can be successfully and energy-efficiently synthesized for 3 h holding time at 700 °C, which represents both a lower temperature and shorter duration compared to the previously reported calcination condition of 900 °C for 12 h.[21]

Electrochemical properties of the phase-pure LTVO sample synthesized under the optimized calcination conditions were further examined in Li cells (Fig. 1c). The as-prepared sample delivers a relatively small reversible capacity of only ~100 mA h g^{-1}, and this electrode performance is inferior compared to that of nanosized LTVO.[21] The layered and cation ordered LTVO oxide is known to transform into a cation-disordered rocksalt structure after Li extraction, resulting in slower kinetics as electrode materials. Therefore, the particle size of the samples synthesized by calcination from conventional oxide-based precursors with lithium carbonate is not sufficiently small, and particle size reduction and surface area increase through post-treatment processes are necessary.[25] In this study, to reduce particle size and enhance electrode kinetics of LTVO, a ball milling treatment was conducted by using a planetary mill.[26,27] Fig. S5 presents XRD patterns and SEM images of ball-milled samples with acetylene black (AB) under different experimental conditions. The XRD patterns of the samples show peak broadening associated with particle size reduction and lowered crystallinity as the rotation speed of ball milling is increased. However, the samples ball-milled at 280–600 rpm for 6 h retain the original layered structure. In contrast, further high-energy ball milling (600 rpm for 12 h) induces a phase transition from layered rocksalt to the disordered rocksalt structure. Fig. S6 displays the XRD patterns of the samples ball-milled at various rotation speeds for 12 h. The original layered structure is retained after ball milling at a relatively low speed of 280 rpm, but cation ordering is gradually lost and disordering is more pronounced on increasing the rotation speed to 450 rpm. These observations indicate that not only ball milling duration but also applied energy are critical factors influencing the phase transition. Fig. 1c shows galvanostatic charge/discharge curves for the ball-milled samples. The discharge capacities increase with both higher rotation speeds and longer milling durations; the samples ball-milled at 280 rpm for 6 h, 450 rpm for 6 h, and 600 rpm for 12 h deliver discharge capacities of 220, 255, and 310 mA h g^{-1}, respectively. In contrast, a different trend is observed for the initial charge capacity. The sample ball-milled at 450 rpm for 6 h exhibits a large capacity of 285 mA h g^{-1}, whereas the high-energy ball-milled (600 rpm for 12 h) sample shows a smaller initial charge capacity of 250 mA h g^{-1}. Moreover, this initial charge capacity is smaller than the initial discharge capacity (310 mA h g^{-1}). This result suggests the partial oxidation of the

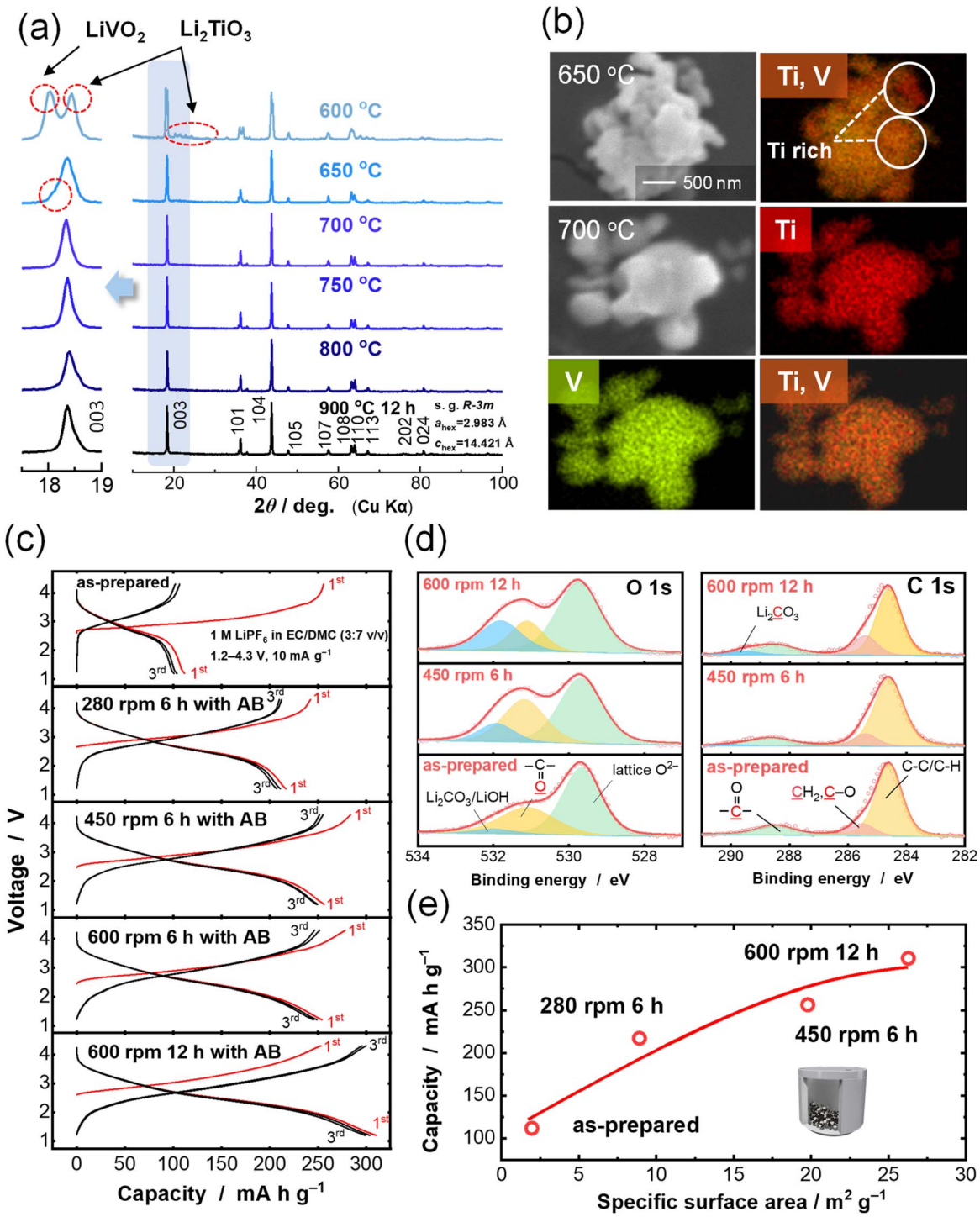

Fig. 1 Synthesis and dependency of electrochemical properties of $Li_{8/7}Ti_{2/7}V_{4/7}O_2$ (LTVO) on particle size: (a) XRD patterns of samples calcined at different temperatures; (b) SEM images and EDX maps of LTVO calcined at 650 and 700 °C. (c) Galvanostatic charge/discharge curves of LTVO prepared under various ball milling conditions. (d) C 1s and O 1s X-ray photoelectron spectra of as-prepared and ball-milled samples at 450 rpm for 6 h and 600 rpm for 12 h. (e) Correlation between the BET specific surface area and initial discharge capacity of LTVO.

active material during the high-energy ball milling.[21] To study the impact of ball milling energy on sample oxidation, X-ray photoelectron spectroscopy (XPS) analysis was conducted. The C 1s and O 1s spectra of as-prepared and ball-milled samples are shown in Fig. 1d. The O 1s spectra show three peaks corresponding to lattice oxygen (oxide ions) in LTVO, Li_2CO_3/LiOH, and organic contaminants.[28–32] The peak intensity of Li_2CO_3/LiOH remarkably increases after high-energy ball milling, and higher peak intensity is observed for the 600 rpm 12 h sample compared to the 450 rpm 6 h sample. This

observation is also consistent with the increasing Li_2CO_3 peak intensity in C 1s spectra. From these results, partial oxidation of LTVO during high-energy ball milling results in Li loss and the formation of Li_2CO_3/LiOH at the surface. To further optimize the ball milling conditions, samples were ball-milled at 450 rpm for different durations, 3, 6, and 12 h (Fig. S7). Although the sample ball-milled for a longer duration delivers a larger discharge capacity, prolonged treatment for 12 h results in the reduced charge capacity, which is indicative of partial oxidation of LTVO.

From these findings, the impact of ball milling on the electrochemical performance is summarized in relation to the specific surface area of the LTVO samples. The correlation between the initial discharge capacity and specific surface area determined by BET measurements is shown in Fig. 1e. The initial discharge capacity increases monotonically with the specific surface area, which is consistent with trends reported in other Li-rich metal oxides.[33] When the specific surface area reaches ~20 m^2 g^{-1}, the sample delivers a large reversible capacity of ~250 mA h g^{-1}. Although high-energy milling is effective in increasing both surface area and reversible capacity, partial oxidation of LTVO is inevitable. As a result, ball milling at 450 rpm for 6 h is identified as the optimal condition to achieve both large reversible capacity and synthesis efficiency without oxidation.

Electrochemical evaluation of $Li_{8/7}Ti_{2/7}V_{4/7}O_2$ with optimized surface area

To further examine the practical feasibility of LTVO with optimized surface area and particle size, structural evolution was evaluated. *In situ* XRD patterns of LTVO are shown in Fig. 2a and S8a. The 003 diffraction line, which is a characteristic feature of the layered structure, disappears gradually during initial charging, indicating V migration and the loss of ordering of Li/V ions. The 108 and 110 diffraction lines are merged into a single peak, which is assigned to the 202 diffraction line for the disordered rocksalt oxide. The splitting of 108 and 110 lines, originating from structural anisotropy of layered materials, disappears upon delithiation, reflecting the transition into a structurally isotropic rocksalt phase. This structural isotropy provides a unique phase transition during electrochemical cycling. Notably, the 200 and 202 diffraction lines show a near-zero peak shift during charge and discharge, indicating the dimensionally invariable character of LTVO as a high-capacity positive electrode material. Although the phase transition during the initial charge induces a small volume change (~0.50%), volume changes in subsequent cycles are negligible due to the isotropic nature of the disordered rocksalt structure as previously reported in nanosized LTVO.[21] For comparison, the structural evolution of $LiVO_2$ during cycling was also examined by *in situ* XRD (Fig. 2b and S8b). Similar to LTVO, the original layered phase is lost during initial charging, and a disordered rocksalt phase is formed. However, the 202 diffraction line shifts toward higher 2θ angles upon charging, indicating lattice contraction. In many Li insertion materials, the unit cell tends to shrink during charging due to increased effective nuclear charge (*i.e.*, reduced ionic radius) and formation of vacant sites, as observed in stoichiometric $LiVO_2$. However, certain V-based electrode materials can exhibit more complex structural evolution: V ions originally located at octahedral sites migrate to face-sharing tetrahedral sites upon charging, causing lattice expansion through increased repulsive interaction between migrated V ions and surrounding ions.[34,35] Therefore, when these two competing effects cancel each other in materials with an appropriate composition, a dimensional invariable character emerges, as observed in $Li_{8/7}Ti_{2/7}V_{4/7}O_2$.[21] The unique dimensional stability during electrochemical cycling should be advantageous for stable operation of all-solid-state cells with minimal stack pressure (*vide infra*). To assess the long-term cyclability of LTVO, extended cycle tests were performed at a rate of 30 mA g^{-1}. Fig. 2c, d and S9 show charge/discharge curves and capacity retention of Li/LTVO cells cycled in a conventional electrolyte solution (1 M $LiPF_6$ in ethylene carbonate/dimethyl carbonate (EC/DMC)) and a highly concentrated electrolyte solution (HCE; 5.5 M $LiN(SO_2F)_2$ (LiFSA) in DMC). Both cells deliver an initial reversible capacity of 235 mA h g^{-1}. However, despite the dimensional stability during cycling, the reversible capacity of the cell with the conventional electrolyte is decreased to 80 mA h g^{-1} after 100 cycles, corresponding to 35% capacity retention. This degradation is primarily due to the dissolution of V^{5+} ions into the electrolyte solution.[21] In contrast, the cell with HCE retains 73% of its initial capacity even after 100 cycles (Fig. 2d and S9). Additionally, coulombic efficiency is also improved with HCE. The superior cycling stability of LTVO with HCE originates from suppression of V dissolution associated with the limited presence of free solvent molecules in HCE.[36,37] This dissolution issue is expected to be completely eliminated when using inorganic solid electrolytes, and the electrochemical performance of LTVO in all-solid-state cells will be further discussed later. The rate capability of the optimized LTVO sample was also evaluated as shown in Fig. 2e. The sample delivers a discharge capacity of approximately 150 mA h g^{-1} even at a high current rate of 1280 mA g^{-1}, demonstrating excellent rate capability.

Scalable solution-based synthesis of nanosized $Li_{8/7}Ti_{2/7}V_{4/7}O_2$

To further explore an efficient synthesis strategy that avoids ball milling, a solution-based approach was employed to directly prepare LTVO samples with large specific surface areas, as schematically summarized in Fig. 3a. Lithium acetate (CH_3COOLi), vanadium acetylacetonate ($V(C_5H_7O_2)_3$), and titanium oxide acetylacetonate ($TiO(C_5H_7O_2)_2$) were dissolved in ethylene glycol, and the resulting solution was heated at 250 °C to evaporate the solvent, yielding an atomically uniform mixture of Li, V, and Ti ions as confirmed by SEM-EDX mapping. An amorphous phase was obtained after solvent removal (Fig. S10). The acetylacetonate ions serve as chelating agents to stabilize the metal cations in solution, promoting uniform and abundant nucleation sites for LTVO and resulting in the formation of fine primary particles.[38] This precursor was subsequently heated at 400 °C for 3 h, followed by additional calcination at different temperatures ranging from 600 to 900 °C for 3 h under an Ar

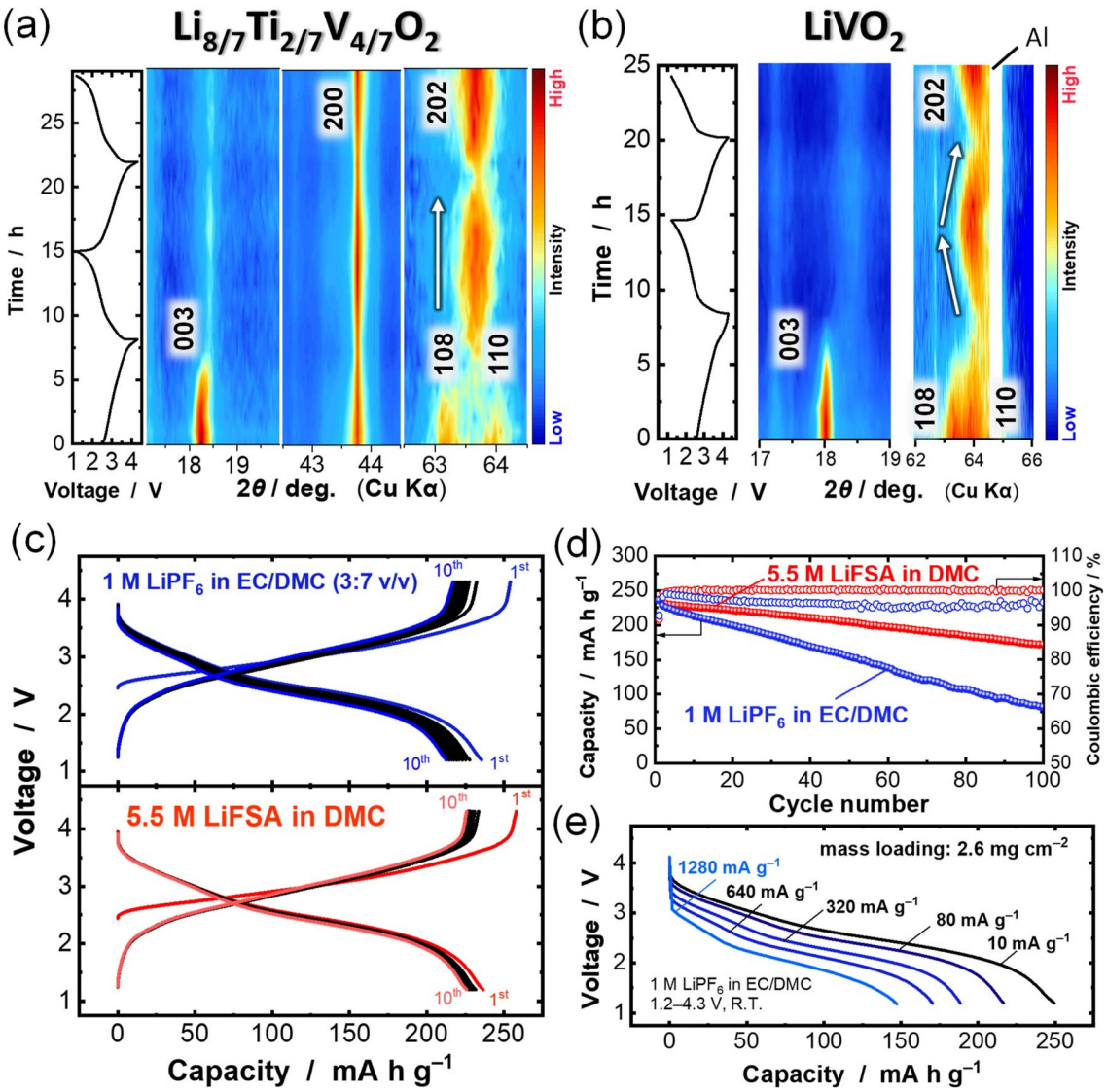

Fig. 2 Phase evolution during charge/discharge and electrochemical properties in different liquid electrolyte solutions: (a) contour plots of *in situ* XRD patterns for the optimized LTVO, (b) $LiVO_2$ electrodes and corresponding charge/discharge curves at 30 mA g^{-1}, (c) galvanostatic charge/discharge curves and (d) capacity retention of optimized LTVO cycled with 1.0 M $LiPF_6$ in EC/DMC and 5.5 M LiFSA in DMC electrolyte solutions at a rate of 30 mA g^{-1}, and (e) rate capability of optimized LTVO with the conventional electrolyte solution.

atmosphere. This method enables the formation of phase-pure and nanosized LTVO samples without requiring post-synthesis ball milling (Fig. S10 and S11). Fig. 3b and S12 compare the XRD patterns and SEM images between LTVO samples synthesized by the solution method and post-ball-milling, both calcined at 700 °C. LTVO synthesized by the solution method exhibits broader diffraction peaks, indicative of lower crystallinity, and consists of smaller nanosized grains than those prepared by the post-ball-milling approach. Furthermore, the BET specific surface area of LTVO synthesized by the solution method is significantly larger than that of the sample prepared by the post-ball-milling approach. N_2 adsorption–desorption isotherms and the corresponding BET surface areas for both samples are shown in Fig. 3c. LTVO synthesized by the solution method after calcination at 700 °C without ball milling exhibits an exceptionally large surface area of 92 m^2 g^{-1}, with even the samples calcined at higher temperatures maintaining surface areas exceeding 80 m^2 g^{-1} (Fig. S13). This extraordinarily large surface area is attributed to the formation of micro/mesopores during calcination, as evidenced by clear hysteresis loops in the adsorption–desorption isotherms.[39,40] Fig. 3d and S14 show galvanostatic charge/discharge curves for LTVO synthesized by the solution method. Owing to its large surface area, the sample calcined at 700 °C without ball milling delivers the highest reversible discharge capacity of 280 mA h g^{-1} at a rate of 30 mA g^{-1}, with negligible initial irreversible capacity.

Practical feasibility of nanosized $Li_{8/7}Ti_{2/7}V_{4/7}O_2$ for sheet-type all-solid-state-batteries operable under minimal stack pressure

To demonstrate a practical benefit of a dimensionally invariable character for LTVO, all-solid-state batteries (ASSBs) with

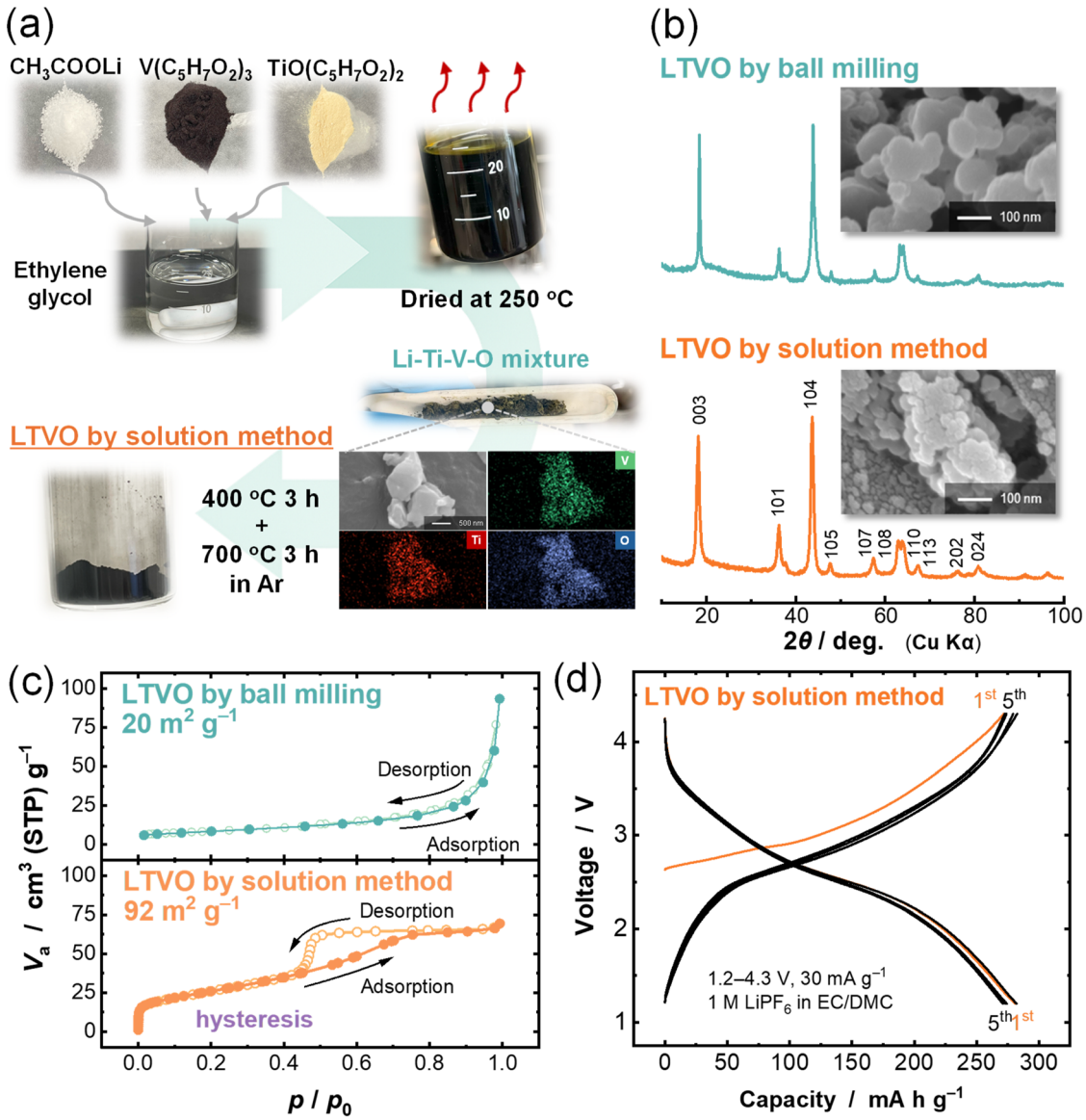

Fig. 3 Solution-based synthesis of LTVO with large surface area: (a) schematic illustration of the solution-based synthesis procedure for LTVO. (b) XRD patterns and SEM images of the optimized LTVO and LTVO synthesized by the solution method. (c) N_2 absorption and desorption isotherms and corresponding BET specific surface area of the respective samples. (d) Galvanostatic charge/discharge curves of LTVO synthesized by the solution method cycled with 1.0 M $LiPF_6$ in EC/DMC at a rate of 30 mA g^{-1}.

a sulfide-based solid electrolyte were assembled. Herein, argyrodite-type $Li_{5.5}PS_{4.5}Cl_{1.5}$ (LPSCl) with a relatively high ionic conductivity (~5 mS cm^{-1}) was used as solid electrolyte.[41,42] The fabrication process of the sheet-type cell is illustrated in Fig. 4a. The cell was fabricated with a three-layer configuration consisting of an LTVO/LPSCl composite positive electrode, LPSCl electrolyte sheet, and Li_xIn alloy negative electrode (Fig. 4b). The composition of the composite electrode was LTVO : LPSCl : VGCF : PVdF-HFP = 47 : 45 : 5 : 3 in wt%. Notably, no liquid electrolyte was added in the all-solid-state configuration. The LTVO sample characterized in Fig. 2 was used for this experiment. A cross-sectional image of the composite electrode is shown in Fig. S15. The composite positive electrode and LPSCl electrolyte sheet are prepared by a conventional slurry method. Cold isostatic pressing (CIP) at 480 MPa was applied to densify the composite electrode and achieve intimate interfacial contact in different layers. The electrochemical performance of LTVO/LPSCl composite electrodes was examined in cells with the same configurations used for liquid electrolytes under minimal pressure. Note that the stack pressure inside the cell, estimated using pressure-indicating films, is below 0.5 MPa, as shown in Fig. 4c. The all-solid-state cell with optimized LTVO delivers a large reversible capacity of 220 mA h g^{-1} at a rate of 50 mA g^{-1} with a minimal stack pressure and achieves considerably superior cycling performance when compared with the HCE (Fig. 4d, e, S9 and S16). Notably, the all-solid-state cell with optimized LTVO demonstrates long-term cycling stability with 90% capacity retention after 270 cycles even at

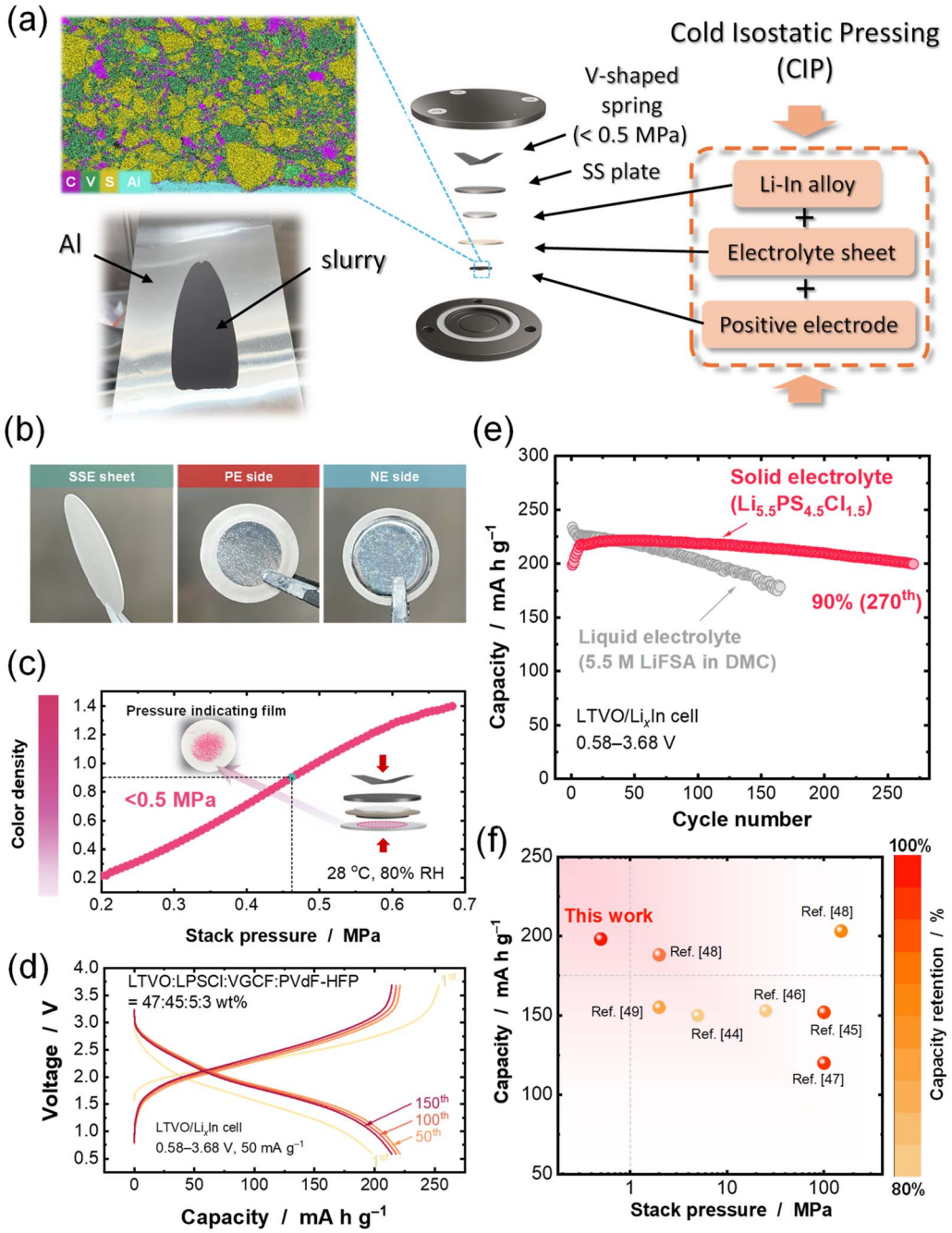

Fig. 4 Preparation and evaluation of all-solid-state batteries with LTVO and a sulfide-based solid electrolyte: (a) schematic illustrations of the fabrication process, a cross-sectional SEM-EDX image of LTVO/LPSCl/VGCF composite electrodes, a photograph of slurry cast on a piece of Al foil, and configurations of the all-solid-state battery operable under minimal stack pressure. (b) Photographs of a solid-state electrolyte ($Li_{5.5}PS_{4.5}Cl_{1.5}$) sheet and all-solid-state cells viewed from the positive electrode (PE) and negative electrode (NE) sides after cold isostatic pressing. (c) Evaluation of stack pressure inside the all-solid-state cell using pressure-indicating films. (d) Galvanostatic charge/discharge curves of the all-solid-state cell with optimized LTVO at a rate of 50 mA g^{-1} at 50 °C, and (e) capacity retention of optimized LTVO cycled with a sulfide-based solid electrolyte ($Li_{5.5}PS_{4.5}Cl_{1.5}$) and a highly concentrated electrolyte solution (5.5 M LiFSA in DMC). (f) Comparison of the initial reversible capacity, capacity retention, and applied stack pressure between the present study and previous reports for all-solid-state batteries with layered-oxide positive electrode materials and sulfide-based solid electrolytes.

a minimal stack pressure (<0.5 MPa) during battery operation, which is attributed to the merit of a near dimensionally invariable character of LTVO. Cross-sectional SEM images of the composite electrodes before and after cycling indicate that the solid–solid interfaces remained intact without crack formation and delamination (Fig. S17a). A stable interface during cycling is also evidenced by the Nyquist plots of the all-solid-state cell (Fig. S17b). Furthermore, the all-solid-state cell delivers

approximately 150 mA h g^{-1} even at a rate of 100 mA g^{-1} (Fig. S18). The all-solid-state cell also delivers a reversible capacity of approximately 200 mA h g^{-1} at room temperature (Fig. S19). To enable scaling up for industrial applications, minimizing stack pressure is essential, with values below 1 MPa generally preferable.[10,43] Fig. 4f and Table S1 summarize the relationship between stack pressure, initial reversible capacity, and capacity retention after 100 cycles in this work and previously reported all-solid-state cells using layered oxide positive electrode materials and sulfide-based electrolytes.[44–49] In most cases, stack pressures exceeding 1 MPa have been applied to suppress void formation arising from the volume changes of layered oxides during cycling. Although a recent study reveals that cells can operate at low stack pressure, their cycling performance is unacceptable due to volume changes.[50] Remarkably, the present cell demonstrates a large reversible capacity exceeding 220 mA h g^{-1} and excellent cycling performance under practically acceptable pressure below 1 MPa. These results clearly demonstrate that the use of dimensionally invariable electrode materials combined with solid electrolytes is a promising strategy toward highly durable and high temperature tolerant rechargeable batteries without high stack pressure. While the mass loading of active materials in this study (2 mg cm^{-2}) is still lower than those reported previously,[48,49] further optimization of the composite electrode, such as increasing the active material fraction and developing functional carbon additives and polymer binders, will enhance practical applicability.

Conclusions

Synthesis conditions of $Li_{8/7}Ti_{2/7}V_{4/7}O_2$ (LTVO), including calcination and ball milling processes, have been systematically studied. A single-phase LTVO sample is successfully obtained at a relatively low temperature of 700 °C with a short heating duration of 3 h. Furthermore, LTVO with the optimum particle size and surface area, ~20 m^2 g^{-1}, is obtained through an efficient post-milling treatment at 450 rpm for 6 h. Additionally, solution-based synthesis successfully produces nanosized LTVO with large specific surface areas without the need for post-milling. The optimized sample delivers a larger reversible capacity with good reversibility in both liquid and solid electrolytes. Particularly, superior reversibility is achieved in the highly concentrated electrolyte with LiFSA because of suppressed V ion dissolution into electrolyte. Moreover, the optimized LTVO sample without surface coating exhibits further improved cycling performance in all-solid-state batteries with sulfide-based solid electrolytes, even under minimal stack pressure, owing to its dimensionally invariable character for LTVO. These findings offer a promising strategy for developing practical all-solid-state batteries that are operable without high stack pressure.

Author contributions

Teppei Ohno: formal analysis, writing – original draft, data curation. Yosuke Ugata: formal analysis, writing – review & editing. Naoaki Yabuuchi: funding acquisition, writing – review & editing, conceptualization.

Conflicts of interest

There are no conflicts to declare.

Data availability

All relevant experimental and theoretical data within the article will be provided by the corresponding author on reasonable request. The data supporting this article have been included as part of the supplementary information (SI). See DOI: https://doi.org/10.1039/d5ta07405c.

Acknowledgements

This work is partially based on the results obtained from a project, SOLiD-Next (JPNP23005), subsidized by the New Energy and Industrial Technology Development Organization (NEDO). NY acknowledges the partial support by JST as part of Adopting Sustainable Partnerships for Innovative Research Ecosystem (ASPIRE), Grant Number JPMJAP2313. NY also acknowledges the partial support from JSPS, Grant-in-Aid for Scientific Research (Grant Numbers 21H04698, 24H02204, and 25K22293).

References

1 H. S. Das, M. M. Rahman, S. Li and C. W. Tan, *Renewable Sustainable Energy Rev.*, 2020, **120**, 109618.
2 W. Li, E. M. Erickson and A. Manthiram, *Nat. Energy*, 2020, **5**, 26–34.
3 K. Liu, Y. Liu, D. Lin, A. Pei and Y. Cui, *Sci. Adv.*, 2018, **4**, eaas9820.
4 Y. Wang, W. D. Richards, S. P. Ong, L. J. Miara, J. C. Kim, Y. Mo and G. Ceder, *Nat. Mater.*, 2015, **14**, 1026–1031.
5 N. Kamaya, K. Homma, Y. Yamakawa, M. Hirayama, R. Kanno, M. Yonemura, T. Kamiyama, Y. Kato, S. Hama and K. Kawamoto, *Nat. Mater.*, 2011, **10**, 682–686.
6 P. Wang, S. Patel, H. Liu, P. H. Chien, X. Feng, L. Gao, B. Chen, J. Liu and Y. Y. Hu, *Adv. Funct. Mater.*, 2023, **33**, 2307954.
7 S. H. Jung, U. H. Kim, J. H. Kim, S. Jun, C. S. Yoon, Y. S. Jung and Y. K. Sun, *Adv. Energy Mater.*, 2020, **10**, 1903360.
8 S. Payandeh, C. Njel, A. Mazilkin, J. H. Teo, Y. Ma, R. Zhang, A. Kondrakov, M. Bianchini and T. Brezesinski, *Adv. Mater. Interfaces*, 2023, **10**, 2201806.
9 S. Puls, E. Nazmutdinova, F. Kalyk, H. M. Woolley, J. F. Thomsen, Z. Cheng, A. Fauchier-Magnan, A. Gautam, M. Gockeln and S.-Y. Ham, *Nat. Energy*, 2024, **9**, 1310–1320.
10 J. Oh, W. J. Chung, S. H. Jung, Y. Kim, Y. Lee, Y. J. Nam, S. Lee, C. H. Kim and J. W. Choi, *Energy Storage Mater.*, 2024, 103606.
11 M. J. Wang, E. Kazyak, N. P. Dasgupta and J. Sakamoto, *Joule*, 2021, **5**, 1371–1390.

12 K. Kawai, H. Lee, Y. Nomura, M. Fujita, H. Kitaura, E. Hosono, H. Nakajima, H. Tsukasaki, S. Mori and A. Sakuda, *ACS Appl. Mater. Interfaces*, 2024, **16**, 57377–57385.
13 C. Xu, J. Feng, S. Sun and X. Zhao, *J. Mater. Chem. A*, 2024, **12**, 14940–14956.
14 X. Zhao, Y. Tian, Z. Lun, Z. Cai, T. Chen, B. Ouyang and G. Ceder, *Joule*, 2022, **6**, 1654–1671.
15 R. Clément, Z. Lun and G. Ceder, *Energy Environ. Sci.*, 2020, **13**, 345–373.
16 J. Lee, A. Urban, X. Li, D. Su, G. Hautier and G. Ceder, *Science*, 2014, **343**, 519–522.
17 N. Yabuuchi, *Curr. Opin. Electrochem.*, 2022, **34**, 100978.
18 S. Hoshino, A. M. Glushenkov, S. Ichikawa, T. Ozaki, T. Inamasu and N. Yabuuchi, *ACS Energy Lett.*, 2017, **2**, 733–738.
19 M. Nakajima and N. Yabuuchi, *Chem. Mater.*, 2017, **29**, 6927–6935.
20 N. Ikeda, I. Konuma, H. B. Rajendra, T. Aida and N. Yabuuchi, *J. Mater. Chem. A*, 2021, **9**, 15963–15967.
21 I. Konuma, D. Goonetilleke, N. Sharma, T. Miyuki, S. Hiroi, K. Ohara, Y. Yamakawa, Y. Morino, H. B. Rajendra, T. Ishigaki and N. Yabuuchi, *Nat. Mater.*, 2023, **22**, 225–234.
22 H. Nagata and K. Kataoka, *Inorg. Chem. Commun.*, 2025, 114299.
23 J. Zheng, P. Yan, L. Estevez, C. Wang and J.-G. Zhang, *Nano Energy*, 2018, **49**, 538–548.
24 N. V. Tarakina, R. B. Neder, T. A. Denisova, L. G. Maksimova, Y. V. Baklanova, A. P. Tyutyunnik and V. G. Zubkov, *Dalton Trans.*, 2010, **39**, 8168–8176.
25 Y. Zhang, Y. Ugata, B. L. Campéon and N. Yabuuchi, *Adv. Energy Mater.*, 2024, **14**, 2304074.
26 R. Qi, B. D. L. Campéon, I. Konuma, Y. Sato, Y. Kaneda, M. Kondo and N. Yabuuchi, *Electrochemistry*, 2022, **90**, 037005.
27 R. Chen, S. Ren, M. Knapp, D. Wang, R. Witter, M. Fichtner and H. Hahn, *Adv. Energy Mater.*, 2015, **5**, 1401814.
28 V. P. Budaev, S. D. Fedorovich, A. V. Lubenchenko, A. V. Karpov, N. E. Belova and M. K. Gubkin, *Heliyon*, 2020, **6**, e05510.
29 Y.-C. Lu, A. N. Mansour, N. Yabuuchi and Y. Shao-Horn, *Chem. Mater.*, 2009, **21**, 4408–4424.
30 N. Schulz, R. Hausbrand, L. Dimesso and W. Jaegermann, *J. Electrochem. Soc.*, 2018, **165**, A819–A832.
31 K. N. Wood and G. Teeter, *ACS Appl. Energy Mater.*, 2018, **1**, 4493–4504.
32 Y. Wu, J. Ju, B. Shen, J. Wei, H. Jiang, C. Li and Y. Hu, *Small*, 2024, **20**, e2311891.
33 Y. Ugata, C. Motoki, T. Handa and N. Yabuuchi, *Solid State Ionics*, 2025, **424**, 116855.
34 M. Nakajima and N. Yabuuchi, *Chem. Mater.*, 2017, **29**, 6927–6935.
35 C. Baur, M.-E. Lacatusu, M. Fichtner and R. E. Johnsen, *ACS Appl. Mater. Interfaces*, 2020, **12**, 27010–27016.
36 J. Wang, Y. Yamada, K. Sodeyama, C. H. Chiang, Y. Tateyama and A. Yamada, *Nat. Commun.*, 2016, **7**, 1–9.
37 Y. Ugata and N. Yabuuchi, *Trends Chem.*, 2023, **5**, 672–683.
38 A. E. Danks, S. R. Hall and Z. Schnepp, *Mater. Horiz.*, 2016, **3**, 91–112.
39 M. Kruk and M. Jaroniec, *Chem. Mater.*, 2001, **13**, 3169–3183.
40 E. Kang, Y. S. Jung, G. H. Kim, J. Chun, U. Wiesner, A. C. Dillon, J. K. Kim and J. Lee, *Adv. Funct. Mater.*, 2011, **21**, 4349–4357.
41 R. P. Rao and S. Adams, *Phys. Status Solidi A*, 2011, **208**, 1804–1807.
42 C. Yu, S. Ganapathy, J. Hageman, L. Van Eijck, E. R. Van Eck, L. Zhang, T. Schwietert, S. Basak, E. M. Kelder and M. Wagemaker, *ACS Appl. Mater. Interfaces*, 2018, **10**, 33296–33306.
43 J. Zhang, J. Fu, P. Lu, G. Hu, S. Xia, S. Zhang, Z. Wang, Z. Zhou, W. Yan and W. Xia, *Adv. Mater.*, 2025, 2413499.
44 J. M. Doux, H. Nguyen, D. H. Tan, A. Banerjee, X. Wang, E. A. Wu, C. Jo, H. Yang and Y. S. Meng, *Adv. Energy Mater.*, 2020, **10**, 1903253.
45 Z. Li, Y. Wang, J. Wang, C. Wu, W. Wang, Y. Chen, C. Hu, K. Mo, T. Gao and Y.-S. He, *Nat. Commun.*, 2024, **15**, 10216.
46 X. Liu, B. Zheng, J. Zhao, W. Zhao, Z. Liang, Y. Su, C. Xie, K. Zhou, Y. Xiang and J. Zhu, *Adv. Energy Mater.*, 2021, **11**, 2003583.
47 S. Luo, Z. Wang, X. Li, X. Liu, H. Wang, W. Ma, L. Zhang, L. Zhu and X. Zhang, *Nat. Commun.*, 2021, **12**, 6968.
48 L. Wang, A. Mukherjee, C.-Y. Kuo, S. Chakrabarty, R. Yemini, A. A. Dameron, J. W. DuMont, S. H. Akella, A. Saha and S. Taragin, *Nat. Nanotechnol.*, 2024, **19**, 208–218.
49 K. Zhou, S. Lu, C. Mish, Y.-T. Chen, S. Feng, J. Kim, M.-S. Song, H. A. Kim and P. Liu, *ACS Energy Lett.*, 2025, **10**, 966–974.
50 H. J. Shin, J. T. Kim, A. Y. Kim, N. Noh, J. Park, C. R. Park, S. Yu, H. Kim, K. Y. Chung and J. M. Yuk, *Adv. Energy Mater.*, 2023, **13**, 2301220.